Reversibly texturing active surfaces with spatial and temporal control

Sourav Chatterjee and Sachin S Velankar

Abstract

Textured surfaces, formed through wrinkling and folding, are observed abundantly in nature. We are especially motivated by the unique capabilities of some species of cuttlefish that camouflage themselves by rapidly switching from smooth to textured skin by expressing protuberances called papillae. Inspired by this, we developed a shape memory alloy–elastomer composite as a platform for reversible surface texture. A shape memory alloy wire embedded in an elastomer is forced to shrink due to Ohmic heating. This shrinkage is used to drive the reversible buckling of a thin stiff film attached to the elastomer surface. The platform is scalable, produces wrinkling patterns in the flip of a switch, operates at voltages under 10 V, and can be operated reversibly over multiple cycles. The amplitude and kinetics of the surface wrinkling are experimentally characterized. The wrinkle patterns appear and disappear in timescales ranging from tens of seconds to as little as a second depending on the voltage actuating the shape memory alloy wire. Finally, this platform can create reversible wrinkle patterns in a spatially reconfigurable fashion, that is, the location of the texture changes can be varied in real time. A two-dimensional shear lag model is developed to establish the important design parameters governing the formation of wrinkles.

Introduction

Living structures in nature, unlike traditionally engineered machines, are often soft, and hence highly adaptive. There has been much interest in bio-inspired designs (Carpi et al., 2011; Lin et al., 2008; Shepherd et al., 2011; Suo, 2012), which mimic the functionalities of such soft machines. Our objective is to create reversible surface textures using soft substrates inspired, in particular, by the unusual abilities of certain species of cephalopods such as octopus and cuttlefish to camouflage themselves by rapidly changing skin texture (Allen et al., 2009; Hanlon, 2007). While textured surface patterning is observed widely in the animal world (Autumn et al., 2000, 2002; Bechert and Bruse, 2000; Bush et al., 2007; Ghiradella, 2010), what is unique about cephalopods is their ability to transition rapidly—within less than a second—between smooth skin and skin with a complex three-dimensional (3D) texture (Allen et al., 2009; Hanlon, 2007). This study demonstrates surfaces based on composites of shape memory alloys (SMAs) and elastomers that develop reversible and spatially reconfigurable wrinkle textures at the flip of a switch. We also elucidate design principles via a two-dimensional (2D) mechanical model.

Such actively tunable surfaces with well-controlled surface topography changes have applications in undulatory locomotion in soft robots (Maladen et al., 2009), smart optical devices (Dong et al., 2006), morphing surfaces in aircraft wings (Thill et al., 2008), actively tuning surface wetting properties in real time (Chung et al., 2007; Lin and Yang, 2009; Zhang et al., 2012), tuning fluid shapes in open channel microfluidics (Khare et al., 2009; Ohzono et al., 2009), creation of localized structural colors (Xie et al., 2010), and spatially selective switchable adhesion (Chan et al., 2008; Lin et al., 2008). Such applications require surfaces which can change topography reversibly over large length scales and small timescales. In this article, we present a design that is capable of reversible actuation over few-second timescales, and thus of direct relevance to surface tuning applications.

Department of Chemical Engineering, University of Pittsburgh, Pittsburgh, PA, USA

Corresponding author:
Sachin S Velankar, Department of Chemical Engineering, University of Pittsburgh, Pittsburgh, PA 15261, USA.
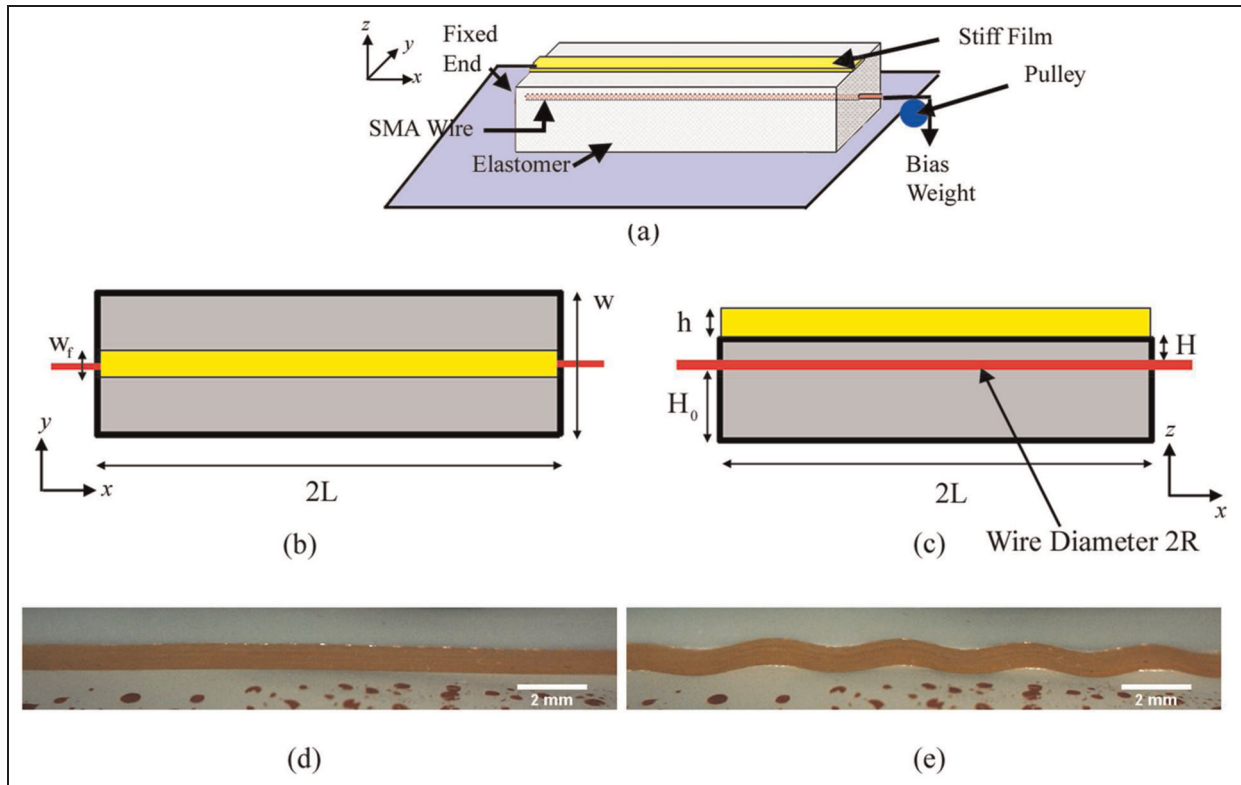Email: velankar@pitt.edu

Figure 1. (a) 3D view of the schematic diagram of the experimental setup. A thin film is attached to a soft elastomer. An SMA wire is embedded in the elastomer. (b) Top view of the schematic. Typical dimensions used in the experiment are $2L = 80$ mm, $w = 20$ mm, and $w_f = 4$ mm. (c) Cross-sectional side view of the setup. The dimensions are highly exaggerated for the purposes of the illustration. Typical dimensions are $h = 25$ μm, $H = 2$ mm, and $H_0 = 20$ mm. (d) A thin polyester film, 25 μm in thickness in its initial non-wrinkled state. (e) Final wrinkled state of the film due to compressive stresses caused by the shrinking of the SMA wire. SMA: shape memory alloy; 3D: three-dimensional.

Previously, textured surfaces have been created through the buckling-induced wrinkling of stiff films attached to compliant surfaces using a wide variety of actuating mechanisms such as thermal stresses (Bowden et al., 1998), solvent diffusion (Chung et al., 2009), volume changes of hydrogels and elastomers (Chan and Crosby, 2006; Tanaka et al., 1987), and shape memory polymers (Li et al., 2012; Xie et al., 2010). However, such wrinkling mechanisms are not easily reversible: once the wrinkle texture is developed, it cannot be smoothed rapidly. Furthermore, while the wrinkle texture can be patterned readily, for example, by lithographic methods (Xie et al., 2010), such spatial patterns are not reconfigurable; it is not possible to make the wrinkle texture appear and disappear at specific locations on command. Very recent work (Agrawal et al., 2012) on reversible wrinkling on liquid crystal elastomer (LCE) substrates is a promising route toward controllable surface texture, although specialized material chemistry is necessary for the LCE sample preparation. Here, we demonstrate a general platform for reversible localized changes in surface texture using a setup that is simple, robust, and scalable across a wide range of length scales. To our knowledge, this is the first

implementation of a rapid, reversible, and reconfigurable change in surface texture at the flip of a switch for eventual applications for smart skins.

The essential idea is to use actuators embedded in an elastomeric matrix to create compressive strain at the free surface. This surface strain can be used to drive a buckling transition, thus resulting in a change in surface texture as illustrated in Figure 1 and discussed in more detail below. We use SMA wires as actuators. SMAs are smart materials that, when heated, undergo diffusion-less solid transformation from the martensite phase to the austenite phase. SMAs have been widely used as actuators, as artificial muscles for biomimetic design (Rediniotis and Wilson, 2002), and in soft robotics (Kim et al., 2009). They offer the advantages of small sizes, high-force capabilities, low actuation voltages, relatively large reversible deformations (3.5%–8% depending on the conditioning process or "training" of the SMA), and reproducible thermo-mechanical behavior over a large number of activation cycles (Duerig et al., 1990). SMA-reinforced polymer matrices have been used for creating prestressed composites with higher strength (Shimamoto et al., 2004; Sittner et al., 2001), improved impact properties (Lau et al., 2004),

and modifying the frequency response of structures (Baburaj and Matsuzaki, 1994). In most such cases, a fairly rigid polymer is used as the matrix. Elastomeric matrices with embedded SMA wires have been considered (Escher and Hornbogen, 1991) for actuator applications. Here, we will show that SMA–elastomer composites offer broad capabilities for realizing surfaces with rapid, reversible, and spatially controllable texture.

Methods and materials

A schematic of the experimental setup is shown in Figure 1(a) to (c). It consists of an SMA wire, held under tension by a dead load bias force, embedded in an elastomer matrix. A thin stiff film is securely attached to the top surface of the elastomer. A potential difference applied across the two ends of the SMA wire causes Joule heating, leading to a martensite-to-austenite transition. The corresponding shrinkage of the SMA wire induces compressive stresses in the stiff film, causing it to buckle and develop a wrinkle texture. The initial unbuckled shape and final buckled shape of the film are shown in Figure 1(d) and (e), respectively. Upon turning off the voltage, the bias force pulls the SMA wire back to its original length and the wrinkle texture disappears. A video (Video_S1.avi) of the entire process is available as Supplementary Information.

SMA wires (Dynalloy, Inc.) of 100 μm diameter were embedded in a room temperature–curing elastomer matrix. Polydimethylsiloxane (PDMS) GI-245 (Silicones, Inc.) was used as the elastomer. From compression testing using the Texture Analyzer (CT3; Brookfield Instruments, Inc.), Young's modulus was found to be 40.7 kPa in the strain range of 0%–3.7%. Since poor interfacial strength is a common problem in SMA–elastomer matrices (Fischer et al., 2011; Jonnalagadda et al., 1998; Jonnalagadda and Sottos, 2000), the SMA wires were coated with beads of silver epoxy (M.G. Chemicals) at roughly few millimeter intervals, which improved bonding strength. The samples were made in a shallow-leveled rectangular mold with the wire being held parallel to the bottom of the mold. The silicone precursor was then poured into the mold in sufficient quantity that the free surface was 2 mm from the wire. The film was placed on the free surface after a few minutes (after the free surface was leveled). Curing the elastomer with the film in place ensured good adhesion, whereas simply placing the film on the elastomer after complete curing sometimes permitted subsequent delamination. With reference to Figure 1(b) and (c), the dimensions were as follows: $2L = 80\,\text{mm}; H_0 = 20\,\text{mm}; H = 2\,\text{mm}; h = 25\,\mu\text{m}; w_f = 4\,\text{mm}; w = 20\,\text{mm}$. During this entire curing process, the wire was held taut by fixing one end and hanging a bias weight of 150 g from the other by means of a pulley. This bias weight enabled reversible actuation by causing the SMA wire to stretch back to its initial length upon cooling. For practical applications, a bias weight is not convenient, and Appendix 1 shows that the same idea may be implemented with mechanical springs instead.

After preparing the samples, a potential difference was applied to the two ends of the SMA wire using a direct current (DC) power supply (Tenma 72-2010). A K-type thermocouple probe, inserted into the soft elastomer and kept in contact with the wire, was used to measure the temperature. The temperature was recorded using a data acquisition system with a NI-9211 thermocouple input module and the Data Acquisition Toolbox in MATLAB. The sample deformation and film profile were monitored using a digital microscope (Dino-Lite Pro AM413T; resolution: 1280 × 1024 pixels, frame rate: 5 frames per second (fps)). Non-contact strain measurements are made using digital image correlation (DIC) methods (Chu et al., 1985; Pan et al., 2009) implemented in MATLAB to track the displacement of ink marks on the elastomer. The camera was mounted inclined at an angle to the elastomer to enable measurement of the height profile at the same time. The height profile could be well-fitted by a sine wave, thus allowing the amplitude and wavelength to be determined.

Experimental results

Geometry and kinetics of buckling

Figure 1(d) and (e) showed the unbuckled and buckled configurations of the SMA–elastomer device at high resolution, respectively. Such images are necessary for the quantitative analysis described below. However, it is also useful to examine the actuation of buckles at a lower magnification (Supplementary Figure S1). It is clear that the entire mid-section of the samples buckles with more-or-less uniform wavelength; however, a significant portion of the sample nearer to the ends does not buckle. Also, most of the wrinkles near the center have a roughly comparable amplitude (at least as may be judged from Figure S1), whereas the outermost wrinkles have a distinctly lower amplitude. Possible reasons for this will be discussed later. In this section, the focus is on quantifying the characteristics of the mid-section of the sample that does buckle.

Video analysis of images such as Figure 1(d) and (e) allows the following parameters to be quantified as a function of time: (1) by fitting a profile of the central two wrinkles to a sinusoid, the wavelength and amplitude can be determined and (2) by DIC of the markers on the elastomer, the strain in the surrounding material can be determined. Moreover, the temperature is monitored simultaneously as a function of time. Figure 2(a) shows the film amplitude and temperature profile measured simultaneously during one complete cycle of excitation and relaxation of the SMA wire at a 6-V
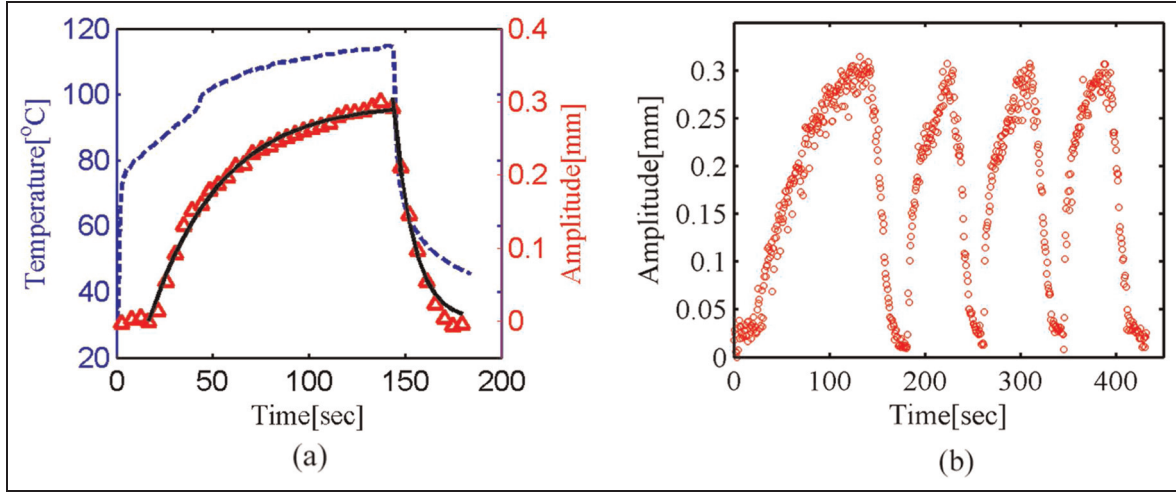
Figure 2. (a) Change of amplitude and temperature with time for *h* = 25 μm polyester film measured simultaneously at an actuation voltage of 6 V. The amplitude is represented by the Δ symbols and the temperature is represented by the dashed line. The black line shows the best fit exponential to the amplitude profile. (b) Amplitude as a function of time, when the device is operated for multiple cycles.

excitation with a current of 0.45 A. (Supplementary video, Video_S1.avi was excited at 8 V resulting in faster actuation. However, most experiments were conducted at a lower voltage to protect against overheating of the wire.) The film remains flat until the SMA reaches its transition temperature (roughly 70 °C quoted by the manufacturer), and subsequently the amplitude nearly follows the growth of the temperature profile.

The sinusoidal fits also gave a wavelength of 3.5 ± 0.2 mm, which was found to remain nearly constant as buckling proceeded. While mechanical stability analysis has not been conducted for this specific situation, we may estimate the wavelength from a plane strain linear stability analysis of an infinitely wide film resting on a softer substrate of infinite thickness (Chung et al., 2011)

$$\lambda = 2\pi h \left(\frac{E_f}{3E_e} \frac{1 - \nu_e^2}{1 - \nu_f^2} \right)^{1/3} \quad (1)$$

While Poisson's ratios have not been measured, we may reasonably set $\nu_e = 0.45$ and $\nu_f = 0.33$. This gives an estimate of 5.3 mm, which is significantly larger than the experimental value of 3.5 mm. This discrepancy may be attributed to the fact that geometry of Figure 1 does not correspond perfectly to an infinitely wide film on a thick substrate. In particular, the SMA wire is only $H = 2$ mm below the film and hence may be expected to resist wrinkling of the film. A somewhat better analog may be of an infinitely wide film bonded to a substrate of finite thickness H for which linear stability predicts (Huang et al., 2005)

$$\lambda = 2\pi h \left(\frac{E_f}{3E_e} \frac{1 - \nu_e^2}{1 - \nu_f^2} \frac{(1 - 2\nu_e)}{(1 - \nu_e)^2} \right)^{1/3} \quad (2)$$

If we set the H to be equal to the distance between the film and the SMA wire, once again with $\nu_e = 0.45$ and $\nu_f = 0.33$, this yields a wavelength 3.2 mm, slightly smaller than the measured value of 3.5 mm. Note, however, that equation (2) is highly sensitive to ν_e, for example, using $\nu_e = 0.46$ would give 3.0 mm. In summary, the wavelength of the wrinkles generated by SMA contraction is comparable to what may be expected from plane strain linear stability analysis of infinitely wide films.

Another quantity of interest is the critical strain for buckling for which linear stability analysis for an infinitely thick substrate (Huang et al., 2005) predicts

$$\varepsilon_c = \frac{1}{4} \left(\frac{3E_e(1 - \nu_f^2)}{E_f(1 - \nu_e^2)} \right)^{2/3} \quad (3)$$

For the experimental values, this gives $\varepsilon_c = 2.2 \times 10^{-4}$. Incidentally, using the critical strain equation for the finitely thick substrate (Huang et al., 2005) gives a comparable value of $\in_c = 3.3 \times 10^{-4}$. These values are too small to be verified by our experimental techniques. Video-tracking experiments of the elastomer surface adjacent to the film strip (Figure 1(d) and (e)) show that the strain in the elastomer surrounding the film is roughly 2.5%, which is somewhat less than the shrinkage of the bare SMA wire. Since this strain far exceeds the critical film strain necessary for buckling, we conclude that the film is far into the post-buckled regime. The amplitude of the wrinkles is theoretically predicted to be (Chung et al., 2011)

$$A = h \left(\frac{\varepsilon - \varepsilon_c}{\varepsilon_c} \right)^{1/2} \quad (4)$$

For the measured strain of about 2.5%, an amplitude of ~0.275 mm is predicted which is in excellent agreement with the data of Figure 2(a) at long times. Next, we turn to the kinetics of the wrinkling process. The typical timescales for wrinkle growth can be obtained by fitting an exponential profile to the amplitude versus time data (as shown in Figure 2(a))

$$A = A_0 \left(1 - \exp\left(\frac{-(t - t_1)}{\tau} \right) \right) \qquad (5)$$

here, t_1 is the time at which the amplitude starts to grow from the initially flat profile. The exponential fit matches the data well and gives a time constant $\tau = 33.7$ s.

On switching off the actuation voltage, the amplitude decays back to 0, that is, the surface texture is completely reversible. The deactuation also follows an approximately exponential decay profile

$$A = A_0 \exp\left(\frac{-(t - t_2)}{\tau} \right) \qquad (6)$$

t_2 is the time at which the SMA is deactuated. For the experiment of Figure 2(a), the time constant was found to be $\tau = 13.0$ s. The amplitude decays completely, and the film reverts to its initial flat state. One consequence of complete reversibility is that the texture change can be applied multiple times with little hysteresis effects, as shown in Figure 2(b). This makes the device useful for applications requiring time-periodic texture formation over multiple cycles. For the experiment of Figure 2(b), the cycle times were controlled manually, using a stopwatch. Later, excitation–relaxation cycles appear to take less time than the first cycle, likely because relaxation only requires the temperature of the wire to drop below the transition temperature, while the elastomer remains warmer than room temperature. Therefore, during the subsequent excitation, the SMA transition temperature can be reached more rapidly. It should be noted of course that complete reversibility of our devices has been tested over only a few cycles. Over much longer cycling, for example, hundreds of cycles, complete reversibility may be compromised by hysteresis effects of the elastomer or the polymer film and the finite fatigue life of nitinol (Duerig et al., 1999).

Dependence of kinetics on actuation voltage

The two timescales involved in the reversible changes in surface texture are the timescales of wrinkle actuation and relaxation. Since the actuation is driven by Joule heating of the SMA wire, it is expected to accelerate with increasing voltage. This is illustrated in Figure 3(a). For an excitation voltage < 5 V (not shown), the surface remained flat indicating that there was insufficient Joule heating to induce shape change in the SMA.

For higher excitation voltages, Figure 3(a) plots the wrinkle amplitude as a function of time. For ease of comparison, the time on the *x*-axis of Figure 3(a) is shifted so that the time at which the amplitude starts to grow is taken as $t = 0$. At all voltages, the amplitude growth may be reasonably well-fitted by an exponential profile (equation (5)). The time constant grows significantly as the voltage reduces toward 5 V. A much higher voltage of 8 V induces far faster actuation, in the order of just 1 s as seen in Supplementary video (Video_S1.avi). However, in order to protect the wire against overheating, most of the experiments were performed at a lower voltage. Thus, while we can achieve actuation times in the order of tens of seconds easily, faster actuation is limited by the inherent difficulty of the SMA to achieve ultra-fast actuations without overheating or breaking the wire. This limitation may be overcome using smart materials capable of faster actuation while still providing large strain, for example, dielectric elastomers or LCEs (Agrawal et al., 2012).

While the actuation voltage affected the kinetics significantly, it had no measurable effect on the wavelength suggesting that the wavelength is not determined by kinetics, but by the equilibrium mechanics of the buckling of a stiff film bonded to a compliant substrate. Within the range of voltages examined, the final value of the amplitude increased with the excitation voltage. This is likely due to a small increase in the strain developed in the SMA, which raises the amplitude as per equation (6).

Next, we turn to the relaxation response. Relaxing the wrinkles back to the flat state requires cooling the SMA wire so that it stretches back to its original length. Accordingly, the relaxation rate depends on the final temperature of the device before deactuation. Figure 3(b) shows the relaxation response of the system for different final temperatures realized by actuating the system at a fixed same actuation voltage of 6 V for different times. The cooling rate depends on the heat transfer characteristics of the system. Hence, assuming a constant heat transfer coefficient, a higher temperature prior to relaxation requires more time to cool the system, and consequently, to reduce the amplitude as apparent in Figure 3(b). Equation (6) can fit the data reasonably well suggesting an exponential decay of amplitude, although admittedly for the data corresponding to 95 °C, the amplitude decay is captured by only three points. These fits give a relaxation time of $\tau = 4.34$ s for an initial temperature of 105 °C, which increases to $\tau = 13.0$ s for an initial temperature of 115 °C. Forced convection or a lower ambient temperature may be expected to accelerate relaxation, although we have not tested this.

Spatially localized wrinkles

The same SMA–elastomer composite platform can readily accomplish spatially reconfigurable surface texture. To produce localized surface wrinkles, the
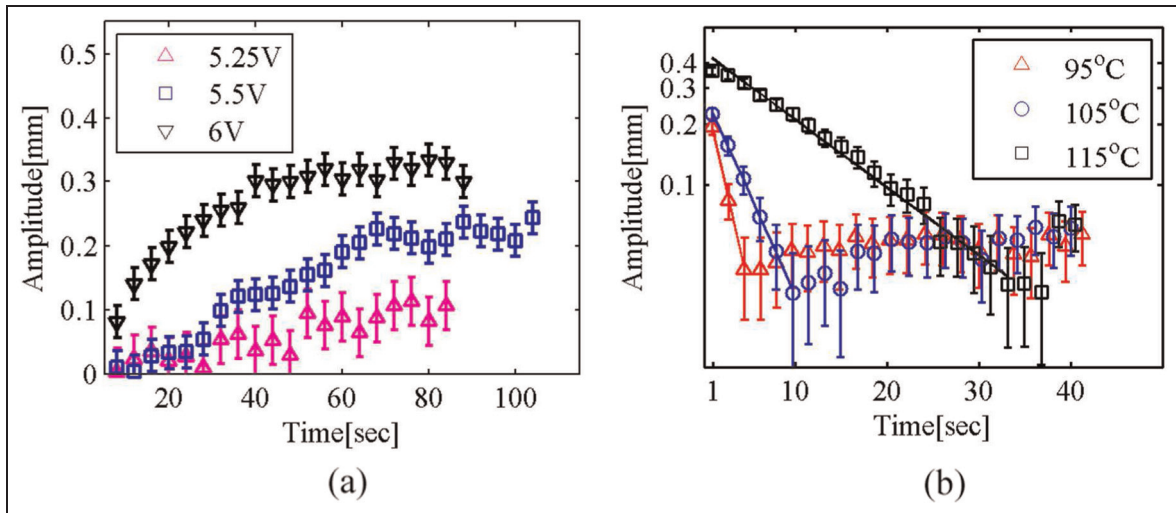
Figure 3. (a) Change of amplitude of wrinkles with time after excitation, for several excitation voltages. The zero time starts from the point where the film buckles and there is a non-zero amplitude. (b) Change of amplitude with time for various final temperatures during the cooling cycle, plotted on a semilog plot.
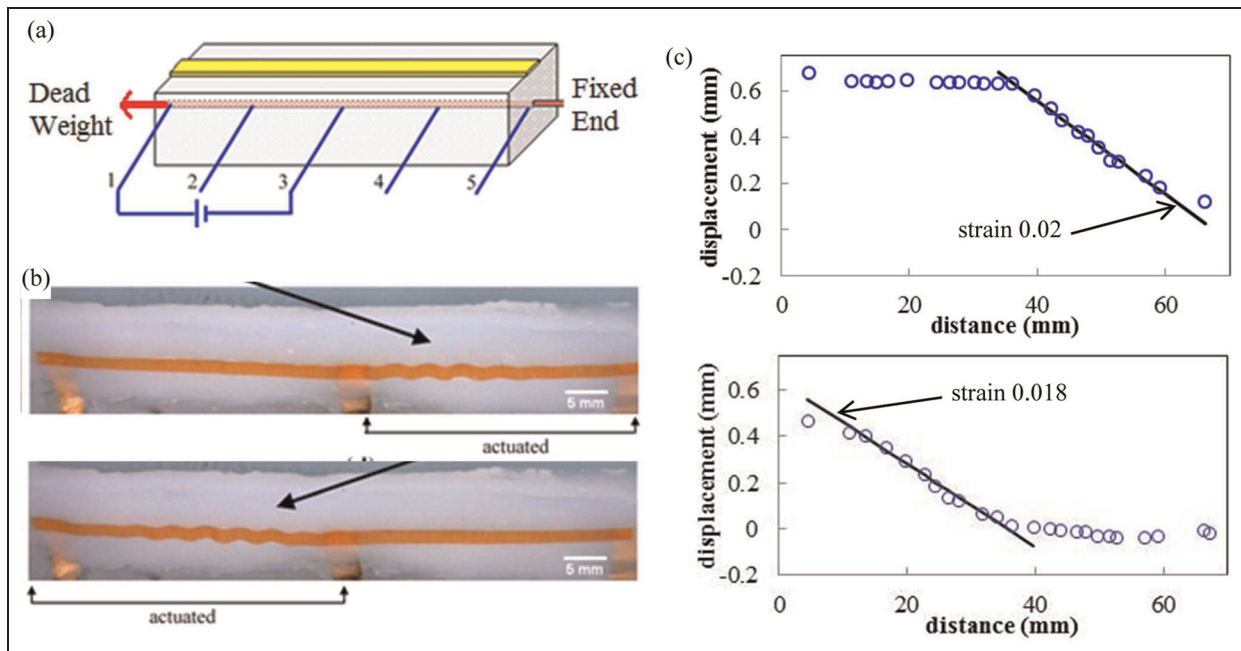

Figure 4. (a) Schematic of excitation setup for spatial control of wrinkling. (b) Wrinkling due to partial excitation of right or left half of the film. (c) Displacement as a function of distance for experiments in (b). The solid lines correspond to regions undergoing strain (2% and 1.8%, respectively).

experimental setup and fabrication procedure were modified as follows: compared to Figure 1(a) where the electrical connections to the SMA wire were made on the portion of the wire outside the sample, in Figure 4(a) the connecting wires were embedded in the matrix at intermediate positions. Adhesive copper tapes, 25 μm thick, were wrapped around the wire and then crimped with relatively more rigid copper strips to make robust electrical connections. Accordingly, different sections of the SMA wire could be addressed by

electrical connections at intermediate positions in the device. Figure 4(b) shows the wrinkle patterns developed upon actuation of the left or right halves of the same sample in a single experiment. Wrinkles are formed only within the actuated regions, while the rest of the sample remains flat. Figure 4(c) quantifies the displacement of the elastomer at the surface obtained from DIC analysis. The slope of the displacement versus position, which is the local strain, changes from near zero in the unactuated region to ~0.02 in the

actuated region. Note that in Figure 4(c), even the non-actuated part of the wire has non-zero displacement because it is pulled by contraction of the actuated part of the wire. However, the displacement in the non-actuated region is spatially uniform and there is no strain. With manual actuation, it is possible to rapidly (within less than 1 min) change the location of the wrinkles by actuating different parts of the SMA wire. With automation and with higher voltage, the wrinkle reconfiguration speed may be accelerated considerably.

The spatial resolution possible is constrained by the limitations of our fabrication (manual crimping connections) which lead to minimum spacings of around 10 mm. While this distance could be reduced significantly by better fabrication methods, a second consideration limiting the spatial resolution is the effect of heat transfer: conduction of heat may lead to shrinkage of the SMA wires immediately adjacent to the actuated region. Finally, the 2D model developed in the following section also suggests that the film can experience strain even outside the length of SMA that is actuated, which may also limit the spatial resolution.

Incidentally, one may also realize spatially localized wrinkles by simply placing the stiff film at specific locations on the surface or by suitably patterning the film modulus. In that case, the buckles would be spatially localized even if the entire SMAs were actuated. Of course, such an approach does not allow reconfigurable texture, that is, the ability to change the location of wrinkles.

Finally, while we have illustrated the basic principles of localized buckling using a single embedded wire, multiple parallel wires may be embedded so that such texture can be realized over a wide surface. In this research, bias weights were used to ensure the reversibility of the surface texture. However, with the use of two-way trained SMA wires (Hebda et al., 1995) or mechanical springs (as shown in Appendix 1), reversible actuation may be realized without bias weights.

Shear lag model

To summarize the experimental portion, we have shown that SMA wires embedded in elastomers can be used to drive a surface buckling transition to permit rapid, reversible, and reconfigurable changes in surface texture. The geometric characteristics of the buckles, for example, wavelength and amplitude, can be estimated from linear stability analysis. Finally, for the specific device configuration used here, there is a zone near the ends of the device where buckles do not appear.

We now turn to modeling the mechanics of the device. The chief goal of the modeling is to identify the appropriate non-dimensional parameters useful in device design, particularly in deciding whether buckles will appear given a set of geometric and material parameters. It is noteworthy that the analysis is valid not just for SMAs but also for any embedded actuators that seek to create a surface strain.

The overall approach is to calculate the strain profile in the film assuming buckling did not happen. Regions where the calculated strain exceeds the expected critical strain for buckling can then be identified as the buckling regions. The analysis is similar to the Volkersen (1938) shear lag model, used for the prediction of adhesive strength in single lap joints. This analysis assumes 2D plane strain conditions that are obviously different from Figure 1(a); however, this approach yields closed-form analytical solutions that are tremendously useful in identifying the effect of the material properties and geometric parameters on the mechanics. Furthermore, since the goal is to predict the strain in the film, we ignore the effect of the solid substrate, which is strictly valid only in the limit of large H_0.

Similar to previous studies (Lagoudas and Tadjbakhsh, 1992), the shape memory effect is modeled by imposing a prestrain $-\varepsilon_{SMA}$, representing the stress-free shape recovery on heating. In the first analysis, prestrain is taken to be constant everywhere, analogous to Figure 1; later we will comment on ε_{SMA} being position-dependent, analogous to Figure 4. Due to constraints from the elastomer and the film, a self-equilibrated internal stress develops, and the prestrain is only partially recovered. In this analysis, the stress-free prestrain is assigned a value $\varepsilon_{SF} = 0.035$:

$$\varepsilon_{SMA}(x) = \varepsilon_{SF} \text{ at all } x \qquad (7)$$

In the following equations, the subscript f refers to the film, the subscript e refers to the elastomer, and the subscript w refers to the wire; u is the displacement, E is Young's modulus, ν is Poisson's ratio, and G is the shear modulus ($G = E/2(1 + \nu)$). The geometric parameters h, H, R, and L are explained in Figure 1(b) and (c). The dimension H_0 is assumed to be sufficiently large so that the solid surface supporting the composite does not affect the mechanics. Equilibrium of forces on a differential element of the film leads to the following differential equation for scaled film displacement $\bar{u}_f$ (where $\bar{u}_f = u_f/h$ and $\bar{x} = x/L$)

$$\frac{\partial^2 \bar{u}_f}{\partial \bar{x}^2} = K_1 \bar{u}_f - K_2 \qquad (8)$$

where K_1 and K_2 are given by

$$K_1 = \frac{L^2}{Hh} \frac{G_e}{E_f} \left(\frac{hE_f}{2RE_w} + 1 \right) \qquad (9)$$

$$K_2 = \frac{L^2}{Hh} \frac{G_e}{E_f} \varepsilon_{SMA} \left(\frac{L}{h} \right) \qquad (10)$$

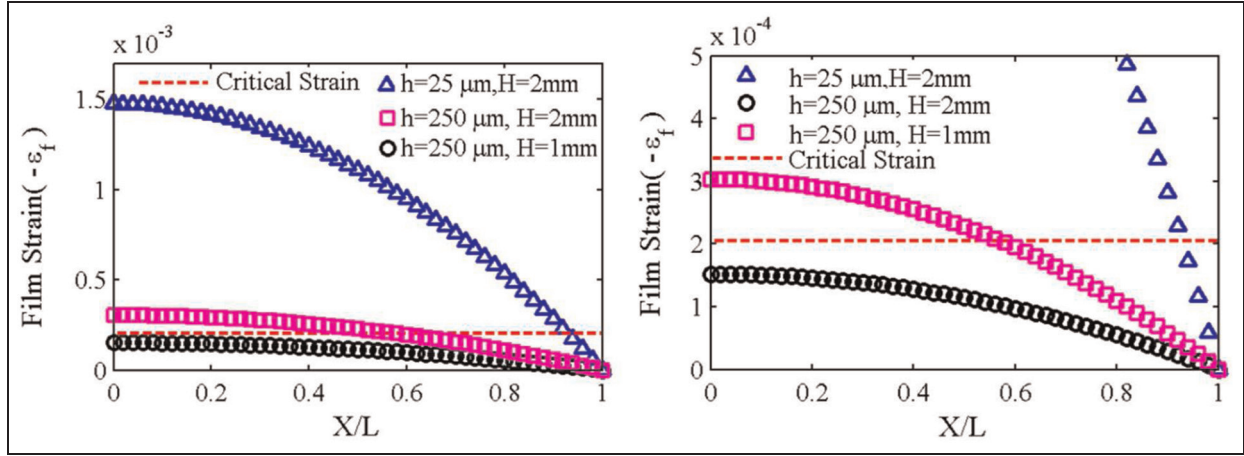The full derivation of these equations is given in Supplementary Information. These equations identify

Figure 5. Magnitude of the compressive strain in the film as a function of position for varying film thicknesses (*h*) and distance between the elastomer and the wire (*H*). The two graphs are identical except that the graph on the right has a magnified *y*-axis. $L = 40$ mm; $E_f = 5$ GPa; $E_e = 39$ kPa; $E_w = 75$ GPa, and $\epsilon_{SMA} = 0.035$. The values of *h* and *H* are as per the legend.

the non-dimensional parameters relevant to mechanics: the geometric parameters hH/L^2, L/h, and $h/2R$ and the material parameters E_f/E_w and E_f/G_e. We solve equation (8) analytically with suitable boundary conditions (see Supplementary Information) to obtain $\bar{u}_f$. The corresponding in-plane displacement in dimensional form is

$$u_f = h\frac{K_2}{K_1}\left[\frac{x}{L} - \frac{\sin h\left(\frac{\sqrt{K_1}x}{L}\right)}{\sqrt{K_1}\cos h\left(\sqrt{K_1}\right)}\right] \quad (11)$$

The derivative $\partial u_f/\partial x$ gives the compressive strain in the film

$$\varepsilon_f = \left(\frac{h}{L}\right)\frac{K_2}{K_1}\left(1 - \frac{\cos h\left(\frac{\sqrt{K_1}x}{L}\right)}{\cos h\left(\sqrt{K_1}\right)}\right) \quad (12)$$

This strain profile is plotted in Figure 5 for the parameter values listed in the caption.

Before proceeding, it must be reiterated that this strain profile is calculated assuming plane strain conditions and assuming that the solid surface on which the entire device rests does not affect the results. We have conducted limited numerical simulations of the exact simulation geometry in 3D without making these assumptions. These simulation results, presented briefly in Supplementary Information, confirm that the strain profile is essentially identical to that predicted by equation (12). Furthermore, we have also conducted several simulations with a variety of parameter values selected such that the maximum strain predicted from equation (12) (i.e. equation (13) below) was held fixed. These simulations confirm that the strain profile changes only modestly. In summary, the numerical simulations strongly suggest that the shear lag analysis correctly

identifies the dimensionless parameters that capture the mechanics of the device.

The strain profiles of Figure 5 lay the basis for identifying the region within which wrinkles happen. Specifically, wrinkles are expected in the region where the compressive strain exceeds the critical strain (estimated from equation (3)), illustrated by the dashed line. Thus, the film is most likely to wrinkle near the middle where the strain is largest. At the ends, the film strain must drop to 0, and hence, near the ends, there must be a zone where the compressive strain is insufficient to produce wrinkles. This is one possible reason for the wrinkle-free zone to be observed experimentally (Supplementary Figure S1). Finally, since the strain reduces, the wrinkle amplitude near the ends is expected to reduce as well, which is also evident in Supplementary Figure S1.

The condition for wrinkles to appear at all requires that the maximum strain $\varepsilon_f^{\max}$ at $x = 0$ exceeds the critical value ε_c for buckling. The maximum strain is the strain value from equation (12) evaluated at $x = 0$

$$\varepsilon_f^{\max} = \left(\frac{h}{L}\right)\frac{K_2}{K_1}\left(1 - \frac{1}{\cos h\sqrt{K_1}}\right) \quad (13)$$

The parameter K_1 is small (0.09) under our experimental conditions, and hence, retaining only terms that are first order in K_1, the previous equation becomes

$$\varepsilon_f^{\max} = \left(\frac{h}{L}\right)\frac{K_2}{2} \quad (14)$$

The critical condition $\epsilon_f^{\max} > \varepsilon_c$ can be approximated by

$$\frac{1}{2}\varepsilon_{SMA}\frac{L^2}{Hh}\frac{G_e}{E_f} > \varepsilon_c \quad (15)$$

We emphasize that equations (14) and (15) are approximations that assume that K_1 is small; if not, equation (13) must be compared with the critical strain. Equation (15) provides insight into the geometric and material parameters that determine whether wrinkling will happen or not. First, increasing film thickness or film modulus increases the bending stiffness of the film, thus inhibiting wrinkling. Second, decreasing elastomer modulus or increasing the elastomer thickness H weakens the shear coupling between the film and the wire, therefore also inhibiting wrinkling. In effect in this latter case, the elastomer deforms readily as the wire shrinks, but does not transmit sufficient stress to induce wrinkles in the film. From an experimental point of view, this implies that stiffer elastomers will be able to transmit greater compressive stress and be able to force buckling even if the surface film has high bending stiffness. However, stiffer elastomers also lead to a higher critical buckling strain, for instance, equation (3) predicts $\varepsilon_c \propto E_e^{2/3}$. Hence, the choice of elastomer is a trade-off between the effectiveness of stress transfer from the SMA to the film versus keeping the critical buckling strain at a low value. In the experimental work above, we have used a fairly compliant elastomer ($E_e = 40$ kPa) chiefly for experimental convenience: a small G_e value yields a large wavelength for the wrinkles making the wrinkle amplitude easier to quantify. Finally, reducing the length of the device is predicted to increase the extent of the end zones where critical strain is not reached. Thus, as mentioned in section "Spatially localized wrinkles," if one seeks to localize wrinkles by simply placing the film at discrete locations, equation (15) predicts the minimum length of the film needed to ensure that buckles appear near the center.

Finally, we observe from equation (11) that $l_f = L/\sqrt{K_1}$ appears as a natural length scale in this problem. Indeed, this is evident even from the original differential equation (8) itself, where K_1 appears as the coefficient to the homogeneous term on the right-hand side. This same length scale l_f would also appear if only a portion of the SMA was to be excited for spatially localized wrinkles. In that case, the homogeneous part of equation (8) would remain unchanged, whereas the second term on the right-hand side would have to be modified so as to capture the actuated region of the SMA wire. This quantity $l_f = L/\sqrt{K_1} = (hHE_f/G_e[(hE_f/2RE_w) + 1]^{-0.5})$ is independent of the length of the film and quantifies the length scale over which strain gradients are sustained in the film; for the specific parameters in our experiment, $l_f \approx 12$ mm. The relevance of this length scale is that if the SMA wire is actuated over a length scale much less than l_f, the strain field will still propagate beyond that region, and hence, buckles might appear even in regions that are not actuated. Thus, apart from fabrication limitations or heat conduction effects, the shear lag model also predicts an inherent mechanical limitation to the resolution with which buckles can be realized. This conclusion applies not just to SMAs but broadly applicable to any type of embedded actuator that seeks to create surface strain in a similar geometry.

It is difficult to quantitatively compare our experiment with the theory. One obvious discrepancy is that the theoretical model assumes 2D plane strain conditions. There are also experimental difficulties with precisely identifying whether buckling has happened or not (buckles of very small amplitude are difficult to identify), thermal effects may be significant (the polymer film or the elastomer may change modulus as the SMA causes heating), and our fabrication method has limited ability to change the materials used. Nevertheless, limited experiments confirm the expected trends qualitatively: increasing the film thickness to 50 μm makes the buckles much weaker, and reducing the distance between the wire and the elastomer reduces the non-buckling zone near the film ends.

We conclude this section by summarizing the advantages as well as limitations of the analytical model. The advantages are that it identifies relevant non-dimensional parameters that control the design of wrinkling surfaces, provides a simple expression (equation (15)) that predicts whether wrinkling happens or not, provides an explicit analytical expression (equation (12)) for the strain profile, and provides a possible explanation for why buckles do not appear near the ends of the film. Furthermore, the analysis would remain valid even if other actuation mechanisms, for example, piezoelectric thin films, carbon nanotube actuators, or electroactive polymers, were embedded in the elastomer instead of SMA wires. Finally, while we were concerned with buckling surfaces (and hence compressive deformations), the exact same strain profile would still remain valid if the actuator expands to induce a tensile strain.

One obvious limitation of the shear lag analysis is that it assumes plane strain conditions. Although in the present situation, the magnitude of the strains predicted by the 2D model is comparable to full 3D simulations, this is fortuitous (see Supplementary Information), and in general, the 2D model will not be able to predict the strain values correctly. Nevertheless, the plane strain analysis is at least qualitatively correct: the shape of the strain profile (i.e. $\varepsilon_f(x)$) is captured correctly and the dependence on geometric and material parameters is approximately captured by K_1 and K_2. A more significant limitation is that the shear lag analysis and the final strain profiles such as in Figure 5 are calculated assuming that buckling does not happen. Once buckles appear, the strain profile is expected to change dramatically within the buckled region. Specifically, since the film cannot sustain a strain far in excess of the critical value, instead of the parabolic profiles of Figure 5, the strain profile is expected to be nearly flat throughout the buckled region at a value nearly equal to the critical

value. Moreover, the buckled region may allow partial relaxation of the strain in the unbuckled region as well. Thus, the shear lag analysis is useful only to identify conditions under which buckling may be expected, but does not extend at all to the post-buckled region. Indeed, this is not just a limitation of the shear lag analysis, it is a limitation of any method—including 3D simulations—that calculates strains using the unbuckled situation. A more detailed analysis in the post-buckling regime would be necessary to predict the final buckled geometry comprehensively.

Conclusion

In summary, we have demonstrated a simple and robust experimental platform for surface texturing, which is spatially reconfigurable and reversible at the flip of a switch. The wrinkle wavelength and amplitude appear to be in reasonable agreement with previous linear stability predictions for compression of stiff films attached to finitely thick compliant supports. Our plane strain model offers straightforward design guidelines for identifying the geometric and material parameters under which wrinkling can happen. Even though the compressive strain at the free surface is relatively small (less than 5%), by harnessing it to drive a wrinkling instability and a simple Euler buckling instability (as shown in Appendix 1), we have been able to realize a significant change in surface texture. The setup is also scalable to smaller length scales by altering the geometry and material properties. The texture is fully reversible, the device can operate for multiple cycle, and the device has response times of as short as a few seconds. Furthermore, we have demonstrated the formation of localized wrinkles through the creation of a non-uniform strain field.

Declaration of conflicting interests

References

Agrawal A, Luchette P, Palffy-Muhoray P, et al. (2012) Surface wrinkling in liquid crystal elastomers. *Soft Matter* 8: 7138–7142.

Allen JJ, Mäthger LM, Barbosa A, et al. (2009) Cuttlefish use visual cues to control three-dimensional skin papillae for camouflage. *Journal of Comparative Physiology: A Neuroethology Sensory Neural and Behavioral Physiology* 195(6): 547–555.

Autumn K, Liang YA, Hsieh ST, et al. (2000) Adhesive force of a single gecko foot-hair. *Nature* 405(6787): 681–685.

Autumn K, Sitti M, Liang YA, et al. (2002) Evidence for van der Waals adhesion in gecko setae. *Proceedings of the National Academy of Sciences of the United States of America* 99(19): 12252–12256.

Baburaj V and Matsuzaki Y (1994) Material damping analysis of a smart hybrid composite lamina. *Journal of Intelligent Material Systems and Structures* 5(5): 647–653.

Bechert D and Bruse M (2000) Experiments with three-dimensional riblets as an idealized model of shark skin. *Experiments in Fluids* 28(5): 403–412.

Bowden N, Brittain S, Evans A, et al. (1998) Spontaneous formation of ordered structures in thin films of metals supported on an elastomeric polymer. *Nature* 393(May): 146–149.

Bush J, Hu D and Prakash M (2007) The integument of water-walking arthropods: form and function. *Advances in Insect Physiology* 34(7): 117–192.

Carpi F, Frediani G, Turco S, et al. (2011) Bioinspired tunable lens with muscle-like electroactive elastomers. *Advanced Functional Materials* 21(21): 4152–4158.

Chan EP and Crosby AJ (2006) Fabricating microlens arrays by surface wrinkling. *Advanced Materials* 18(24): 3238–3242.

Chan EP, Smith EJ, Hayward RC, et al. (2008) Surface wrinkles for smart adhesion. *Advanced Materials* 20(4): 711–716.

Chu TC, Ranson WF, Sutton MA, et al. (1985) Applications of digital image-correlation techniques to experimental mechanics. *Experimental Mechanics* 25: 232–244.

Chung JY, Nolte AJ and Stafford CM (2009) Diffusion-controlled, self-organized growth of symmetric wrinkling patterns. *Advanced Materials* 21(13): 1358–1362.

Chung JY, Nolte AJ and Stafford CM (2011) Surface wrinkling: a versatile platform for measuring thin-film properties. *Advanced Materials* 23(3): 349–368.

Chung JY, Youngblood JP and Stafford CM (2007) Anisotropic wetting on tunable micro-wrinkled surfaces. *Soft Matter* 3(9): 1163–1169.

Dong L, Agarwal AK, Beebe DJ, et al. (2006) Adaptive liquid microlenses activated by stimuli-responsive hydrogels. *Nature* 442(7102): 551–554.

Duerig T, Melton KN, Stockel D, et al. (1990) *Engineering Aspects of Shape Memory Alloys*. London: Butterworth-Heinemann.

Duerig T, Pelton A and Stöckel D (1999) An overview of nitinol medical applications. *Materials Science and Engineering: A Structural Materials Properties Microstructure and Processing* 273–275: 149–160.

Escher K and Hornbogen E (1991) Aspects of two way shape memory in NiTi-silicone composite materials. *Journal de Physique IV* 1(C4): 427–432.

Fischer C, Terriault P and Brailovski V (2011) Debonding characterization of SMA/polymer morphing structures. *Advanced Materials Research* 409: 621–626.

Ghiradella H (2010) Insect cuticular surface modifications: scales and other structural formations. *Advances in Insect Physiology* 38: 135–180.

Hanlon R (2007) Cephalopod dynamic camouflage. *Current Biology* 17(11): R400.

Hebda DA, Whitlock ME, Ditman JB, et al. (1995) Manufacturing of adaptive graphite/epoxy structures with embedded nitinol wires. *Journal of Intelligent Material Systems and Structures* 6(2): 220–228.

Huang ZY, Hong W and Suo Z (2005) Nonlinear analyses of wrinkles in a film bonded to a compliant substrate. *Journal of the Mechanics and Physics of Solids* 53(9): 2101–2118.

Jonnalagadda K and Sottos N (2000) In situ displacement measurements and numerical predictions of embedded SMA transformation. *Smart Materials and Structures* 9(5): 701.

Jonnalagadda KD, Sottos NR, Qidwai MA, et al. (1998) Transformation of embedded shape memory alloy ribbons. *Journal of Intelligent Material Systems and Structures* 9(5): 379–390.

Khare K, Zhou J and Yang S (2009) Tunable open-channel microfluidics on soft poly(dimethylsiloxane) (PDMS) substrates with sinusoidal grooves. *Langmuir* 25(21): 12794–12799.

Kim S, Hawkes E, Choy K, et al. (2009) Micro artificial muscle fiber using NiTi spring for soft robotics. In: *IROS 2009: IEEE/RSJ international conference on intelligent robots and systems*, St. Louis, MO, 10–15 October, pp. 2228–2234. New York: IEEE.

Lagoudas D and Tadjbakhsh IG (1992) Active flexible rods with embedded SMA fibers. *Smart Materials and Structures* 1(2): 162–167.

Lau K, Ling H and Zhou L (2004) Low velocity impact on shape memory alloy stitched composite plates. *Smart Materials and Structures* 13(2): 364–370.

Li J, An Y, Huang R, et al. (2012) Unique aspects of a shape memory polymer as the substrate for surface wrinkling. *ACS: Applied Materials & Interfaces* 4(2): 598–603.

Lin P-C and Yang S (2009) Mechanically switchable wetting on wrinkled elastomers with dual-scale roughness. *Soft Matter* 5(5), 1011–1018.

Lin P-C, Vajpayee S, Jagota A, et al. (2008) Mechanically tunable dry adhesive from wrinkled elastomers. *Soft Matter* 4(9): 1830.

Maladen RD, Ding Y, Li C, et al. (2009) Undulatory swimming in sand: subsurface locomotion of the sandfish lizard. *Science* 325(5938): 314–318.

Ohzono T, Monobe H, Shiokawa K, et al. (2009) Shaping liquid on a micrometre scale using microwrinkles as deformable open channel capillaries. *Soft Matter* 5(23): 4658–4664.

Pan B, Qian K, Xie H, et al. (2009) Two-dimensional digital image correlation for in-plane displacement and strain measurement: a review. *Measurement Science & Technology* 20(6): 062001.

Rediniotis O and Wilson L (2002) Development of a shape-memory-alloy actuated biomimetic hydrofoil. *Journal of Intelligent Material Systems and Structures* 13: 35–49.

Shepherd RF, Ilievski F, Choi W, et al. (2011) Multigait soft robot. *Proceedings of the National Academy of Sciences* 108(51): 20400–20403.

Shimamoto A, Ohkawara H and Nogata F (2004) Enhancement of mechanical strength by shape memory effect in TiNi fiber-reinforced composites. *Engineering Fracture Mechanics* 71(4–6): 737–746.

Sittner P, Michaud V and Schrooten J (2001) Modeling and material design of SMA polymer composites. *Stress* 43(5): 984–993.

Suo Z (2012) Mechanics of stretchable electronics and soft machines. *MRS Bulletin* 37(03): 218–225.

Tanaka T, Sun S, Hirokawa Y, et al. (1987) Mechanical instability of gels at the phase transition. *Nature* 325: 796–798.

Thill C, Etches J, Bond I, et al. (2008) Morphing skins. *Aeronautical Journal* 112(1129): 117–139.

Volkersen O (1938) Die Nietkraftverteilung in zugbeanspruchten Nietverbindungen mit konstanten Laschenguerschnitten. *Luftfahrtforschung*, Deutscher Versuchsanstalt fuer Luftfahrt; Aerodynamischer Versuchsanstalt zu Gottingen; Aerodynamisches Institut der Technischen Hochschule. *Zeitschrift fuer Flugtechnik und Motorluftschiffahrt* 15(1): 41–47.

Xie T, Xiao X, Li J, et al. (2010) Encoding localized strain history through wrinkle based structural colors. *Advanced Materials* 22(39): 4390–4394.

Zhang Z, Zhang T, Zhang YW, et al. (2012) Strain-controlled switching of hierarchically wrinkled surfaces between superhydrophobicity and superhydrophilicity. *Langmuir* 28(5): 2753–2760.

Appendix I

Spring actuation and Euler buckling

Here, we seek to show how the dead load bias weight can be eliminated using a spring. Figure 6 shows a setup that is similar to Figure 1, but with two important differences:

1. The polyester film was placed on the elastomer after curing, and furthermore, a strip of paper was inserted under a portion of the film to ensure that it did not adhere within that region. Thus, the buckling region of the film approximates a beam that is resting—but not attached—to a soft elastomer.

2. Instead of a dead load bias force, the SMA wire was held under tension by a spring. For experimental convenience, the wire was not attached to the spring directly, instead it was threaded through a non-conducting nylon ring and clamped to a nylon screw as shown in Figure 6. The other end of the spring was hooked onto a screw whose position could be adjusted to change the tension in the spring.

The polyester film was approximately flat prior to actuation of the film although some distortion occurred due to the presence of the paper strip. Upon actuation using 3xAA batteries (4.5 V), the portion of the film on
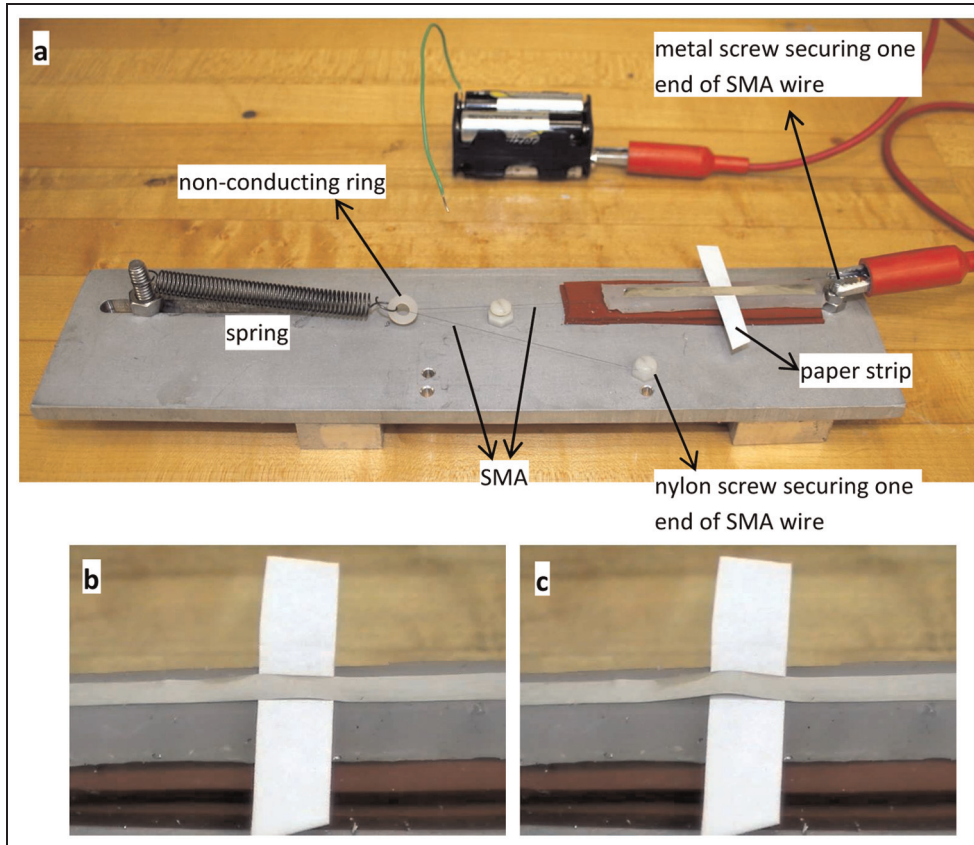
Figure 6. (a) A thin polyester film of thickness *h* = 12.5 μm lies flat, in contact with the elastomer substrate over its entire length except for the paper strip. When the free end of the wire from the battery touches the SMA wire, it induces actuation of the SMA and Euler buckling of the film. (b, c) Close-up views of the polymer film before and after actuation. These images are frames taken from the video file Video_S2.mp4.

the paper strip buckled. The entire process is shown in Supplementary video Video_S2.mp4.

In summary, Figure 6 shows that (1) the SMA–elastomer composite device can drive elastic instabilities other than the wrinkling discussed in the main text, (2) dead load bias can be eliminated readily in favor of springs, and (3) the power requirements to drive the SMA can be satisfied by batteries. The latter two items suggest that such SMA–elastomer devices are suitable for portable applications. However, the significant power dissipation in SMAs may not permit long-duration operation with a battery.